



# Protein hydrogel networks: A unique approach to heteroatom self-doped hierarchically porous carbon structures as an efficient ORR electrocatalyst in both basic and acidic conditions

Liqiang Wang<sup>a,b,c,1</sup>, Kaixin Liang<sup>a,1</sup>, Liu Deng<sup>a</sup>, You-Nian Liu<sup>a,b,\*</sup>

<sup>a</sup> College of Chemistry and Chemical Engineering, Central South University, Changsha, Hunan, 410083, PR China

<sup>b</sup> State Key Laboratory of Powder Metallurgy, Central South University, Changsha, Hunan, 410083, PR China

<sup>c</sup> Key Laboratory of Photochemical Conversion and Optoelectronic Materials, TIPC, CAS, Beijing, 100190, PR China



## ARTICLE INFO

### Keywords:

Protein hydrogels  
Metal-free electrocatalysts  
Heteroatom-doped carbon  
Hierarchically porous carbon  
Oxygen reduction reaction

## ABSTRACT

It is of great allure but still challenging to construct carbon-based metal free electrocatalysts to replace Pt-based ones for efficient ORR in both acidic and alkaline media. In this work, protein-hydrogel networks are demonstrated as a precursor for preparing N, S-codoped, hierarchically porous carbon (NSPC) materials with tunable pore structure. Of note, NSPC-0.2-900 possesses a high pore volume of  $0.8552 \text{ cm}^3 \text{ g}^{-1}$  and shows excellent ORR activity in both alkaline ( $E_{\text{onset}} \sim 0.93 \text{ V vs. RHE}$ ) and acidic ( $E_{\text{onset}} \sim 0.89 \text{ V vs. RHE}$ ) media. As a cathode catalyst for zinc-air batteries, NSPC exhibits higher power density and better long-term durability than Pt/C does. The work presents a great potential of using protein as a precursor for preparing heteroatom doped, hierarchically porous carbon materials for energy and environmental applications.

## 1. Introduction

Seeking efficient electrocatalysts for oxygen reduction reaction (ORR) is of great significance, as it lies at the heart of various energy conversion and storage technologies [1–5]. For example, ORR takes place during the discharge process of Zn-air batteries (ZABs), which have been paid wide attentions owing to their low cost, high energy density, safety, environmental benignity etc. Recently, ZABs are undergoing the development from aqueous-state to solid-state, from rigid-state to flexible-state, and from primary ones to rechargeable ones. Nevertheless, developing high-performance ORR catalysts is still crucial to promote the development of the ZABs [6–10]. Precious metals especially Pt-based catalysts show superior properties and still play an overwhelming role in commercially available ones. However, Pt is of high cost and very scarce in the earth's crust, inevitably restricting the large-scale implementation in renewable energy technologies. In particular, Pt-based catalysts often suffer poor catalytic stability and tolerance to monoxide and methanol [11–15].

Recently, much attention has been shifted to noble metal-free ORR catalysts. Among them, heteroatom-doped carbon materials have gained a lot of attention as an alternative electrocatalyst for ORR [5,13,16–19]. Heteroatoms (e.g., N, S, P etc.) can either work as

catalytic centers themselves or activate the adjacent carbon atoms for ORR catalysis. Since Dai and coworkers reported that N-doped carbon nanotube arrays showed super ORR activity in alkaline condition, considerable endeavors have been devoted to engineering crystalline carbon (e.g., graphene, carbon nanotube etc.) into electrocatalysts for ORR [11]. Though great progress has been made in developing carbon materials as metal-free ORR catalysts, there are still some challenges that need to be addressed before putting them into practical applications. Firstly, highly crystalline carbon structures, such as graphene and carbon nanotube, often suffer  $\pi$ - $\pi$  stacking-induced aggregation, leading to the compromise of active sites [20,21]. Moreover, both the preparation of crystalline carbon and the subsequent introduction of heteroatoms are tedious and costly, which seriously restrains their large-scale preparation and practical applications. In addition, the ORR activity of these carbon materials is still inferior to commercially available Pt/C especially in acidic media, probably due to the acidic medium-induced inactivation or loss of active sites [22–25].

Recently, heteroatom-doped porous carbon materials especially those arising from biomass like polysaccharides and proteins, have gained great interest in energy [26,27], catalysis [16], environment [28,29] etc. The heteroatom dopant is capable of creating efficient active sites, meanwhile the porous structure allows more active sites to

\* Corresponding author at: College of Chemistry and Chemical Engineering, Central South University, Changsha, Hunan, 410083, PR China.  
E-mail address: [liuyounian@csu.edu.cn](mailto:liuyounian@csu.edu.cn) (Y.-N. Liu).

<sup>1</sup> These authors contribute equally to this work.

be exposed, both of which are commendably desired for ORR catalysts [27,30–32]. Of particular, hierarchical pores with collective properties of micropore ( $< 2 \text{ nm}$ ) as a confined reactor, mesopore (2–50 nm) and macropore ( $> 50 \text{ nm}$ ) as a channel of mass transport, ionic conductivity and carbon wetting, are capable of remarkably improving the ORR activities of carbon materials in both acid and alkaline condition. Biomass shows great potential to be engineered into porous carbon in a large scale, owing to its abundant reserves, extremely low cost and unique structure and composition. Especially, most biomass, such as polysaccharide and protein, contains certain amounts of N, S, which makes them potential precursors for fabricating heteroatom-doped carbon structure for ORR [27,33–35]. However, it is still challenging to develop methodologies for facilely fabricating biomass-based, heteroatom-doped carbon materials which can be used as an efficient electrocatalyst for ORR in both acidic and alkaline conditions [31,36].

Hydrogels possess unique network and spatial configuration, which makes them excellent precursors or templates for preparing porous carbon materials. Recently, engineering biomass especially polysaccharides into highly ordered hydrogel networks, has emerged as an effective pathway to prepare porous carbon materials [22,37–40]. For example, Yao and coworkers fabricated porous metal sulfides/carbon aerogels by the carbonization of carrageenan-metal hydrogels [37]. Lately, they developed an N-modified S-defect carbon aerogel with a 3D hierarchical porous structure via annealing the urea-functionalized carrageenan hydrogels. The material exhibited excellent ORR activity in acidic medium [41]. Yu's group demonstrated that bacterial cellulose can be utilized as a precursor to fabricate N-doped porous carbon materials for ZABs [40]. Similar to polysaccharides, protein possesses certain conformations, determined composition and spatial structures, making them a potential precursor for functional carbon materials. Of note, most protein molecules contain certain amounts of S element that is reported able to be converted into –S–C– or –S–N–C– that possibly work as highly active sites for ORR in acidic medium [42]. In addition, the pore structure of the carbon materials can be regulated via adjusting the structures and compositions of the protein-derived precursors. However, there are few reports on engineering protein hydrogels into metal-free electrocatalysts for ORR [43–45].

In this work, alkali (e.g., NaOH) is found able to drive proteins (e.g., bovine serum albumin) to form hydrogel networks. BSA is a water-soluble globular protein and consists of 583 amino acid residues including 35 cysteine residues, making it as a unique precursor towards self-heteroatom doped carbon. In addition, BSA contains abundant secondary structures, such as  $\alpha$ -helix,  $\beta$ -sheet,  $\beta$ -turn and random coil, allowing them to form unique assembling structure under certain conditions [46,47]. These networks can be engineered into heteroatom (N, S) self-doped, hierarchical porous carbon (NSPC) with tunable pore structures simply via freeze-drying and subsequent carbonizing (Fig. 1a). The pore structure can be tuned from single micropore to the mixed micropore and mesopore, eventually to hierarchical pores by tuning the structure of hydrogel or/and pyrolysis temperature. It is noteworthy that the obtained hierarchically porous carbon materials possess high pore volume ( $0.8550 \text{ cm}^3 \text{ g}^{-1}$ ) and specific surface areas ( $1274 \text{ m}^2 \text{ g}^{-1}$ ), which not only provides large accessible surface areas and consequently more exposed active sites, but also favors the rapid mass transfer for the electrocatalytic process. As a result, the hierarchically porous carbon materials exhibit comparable ORR activity to that of commercial Pt/C in alkaline condition, and remarkably enhanced ORR activity compared with their counterparts. Furthermore, the as-prepared carbon materials display better stability, methanol tolerance, and markedly enhanced ORR properties in acidic media with the onset potential only  $\sim 80 \text{ mV}$  smaller than that of Pt/C. In addition, the carbon-based electrocatalyst exhibits much better stability than that of Pt/C when explored it as an air cathode catalyst for ZABs.

## 2. Experimental section

### 2.1. Materials

Bovine serum albumin (BSA) was purchased from Sinopharm Chemical Reagent Co. (Beijing, China). Without statement, all other chemicals are commercially available and of analytical grade. Milli-Q water was used through the whole experiments.

### 2.2. Preparation of BSA hydrogels and BSA aerogels

In a typical procedure, a pre-required amount of NaOH aqueous (10 M) was added into BSA aqueous solution to obtain BSA hydrogels or BSA solution with different mass ratio of NaOH to BSA. When mass ratio of BSA to NaOH was 0.05 and 0.2, the hydrogel samples were named as NaOH-BSA-0.05 and NaOH-BSA-0.2, respectively. The final BSA concentration is around  $75 \text{ mg mL}^{-1}$ . The obtained BSA was subjected to a freeze-drying process on a freeze drier (Scientz-10 N, Ningbo Biotechnology Co., Ltd, Ningbo, China) over night to make sure that water within the hydrogels was completely removed. After freeze-drying, a porous BSA aerogel is obtained.

### 2.3. Synthesis of N,S-codoped, porous carbon (NSPC)

NSPC samples were obtained by annealing aerogels or BSA powders at pre-set temperature (500–900 °C) under  $\text{N}_2$  atmosphere for 2 h in a tube furnace (OTF-1200X, Kejing Co., Ltd, Hefei, China), followed by ball-milling and ultrasonic cleaning in 1 M hydrochloric acid for 10 h to remove the metal ions such as  $\text{Na}^+$ .

### 2.4. Characterization

TEM images were obtained on an FEI Titan G2 60–300 with spherical aberration correction, and FE-SEM images were obtained with a Helios NanoLab 600i Dual Beam FIB/FE-SEM (FEI, USA). X-ray photoelectron spectroscopy (XPS) analysis was performed on an ESCALAB 250Xi XPS (Thermo Fisher, USA). Powder X-ray diffraction (XRD) patterns of the samples were measured on a Rigaku D/max 2550 X-ray diffractometer with  $\text{Cu K}\alpha$  radiation ( $\lambda = 0.15418 \text{ nm}$ ) (Japan). Nitrogen adsorption-desorption isotherms were measured using an ASAP 2020 surface area and a pore analyzer (Micromeritics Instruments, USA). Raman spectra were obtained on Renishaw RM1000 confocal Raman spectrometer (Renishaw, UK).  $\text{CO}_2$ -TPD was performed on micromeritics (AutoChemII2920, USA). Circular dichroism (CD) spectra of different samples were tested on a CD spectrometer (Jasco-815, Japan).

### 2.5. Electrochemical measurements

The ORR properties of the obtained NSPC were evaluated on a electrochemical workstation (Pine Research Instrumentation, Inc., Durham, NC, USA). All electrochemical tests were conducted in a three-electrode testing system, using Ag/AgCl electrode as a reference electrode, platinum wire as a counter electrode and glassy carbon electrode as a working electrode. The ORR was performed in 0.1 M  $\text{HClO}_4$  or 0.1 M KOH to evaluate the performance of the electrocatalysts in acidic and alkaline conditions respectively. Working electrodes were prepared as follows: the sample (5 mg) was dispersed in the mixture of 0.5 mL DI water and 0.5 mL ethanol containing 0.1 wt% Nafion, followed by 1 h sonication to obtain a homogeneous suspension. Then, 3  $\mu\text{L}$  of the above obtained catalyst ink was dropped onto the polished glassy carbon electrode (diameter: 3 mm). After solvent evaporation, the working electrode was subjected to the electrochemical test. Linear sweep voltammetry (LSV) was performed on a rotating disk electrode (RDE) with a disk diameter of 5.0 mm in  $\text{O}_2$  or  $\text{N}_2$ -saturated 0.1 M KOH solution or 0.1 M  $\text{HClO}_4$ . The scan rate and rotating rate is  $5.0 \text{ mV s}^{-1}$  and

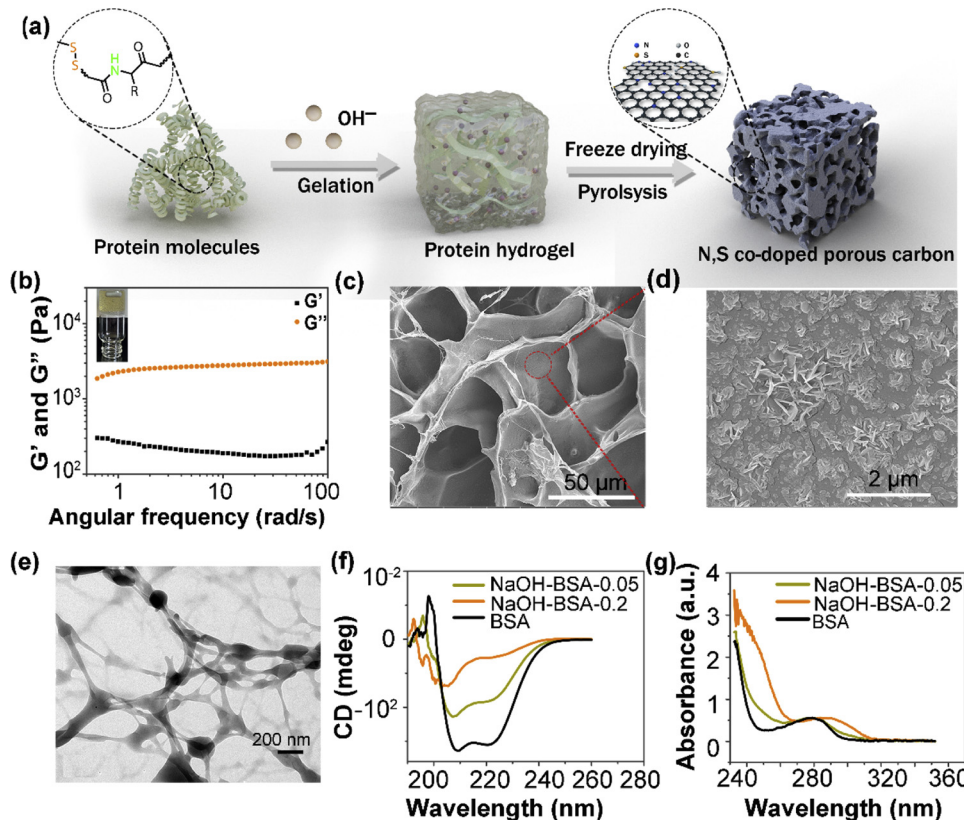


**Fig. 1.** (a) Schematic illustration of using protein hydrogels for construction of hierarchically porous carbon materials. (b) Frequency-dependent (at a strain of 1%) oscillatory shear rheology, the inset presents the image of hydrogels. (c), (d) SEM images, (e) TEM images of the BSA hydrogels (ratio of NaOH to BSA: 0.2). (f), (g) CD and UV-vis spectra of BSA solution respectively, containing different amounts of NaOH.

1600 rpm respectively. The stability of the NSPC-0.2-900 and commercially available Pt/C was measured by chronoamperometric responses at a constant potential of  $-0.1$  V (vs. NHE) in 0.1 M KOH or 0.5 V (vs NHE) in 0.1 M HClO<sub>4</sub> respectively. The crossover effect of methanol for Pt/C and NSPC-0.2-900 were tested as follows: 500  $\mu$ L of methanol was injected into 150 mL of O<sub>2</sub> saturated 0.1 M KOH or 0.1 M HClO<sub>4</sub> solution at around 300 s with an electrode rotation rate of 1600 rpm. Rotating ring-disk electrode (RRDE) test was performed on a RRDE configuration (Pine Research Instrumentation) with a disk electrode (glassy carbon, area: 0.2475 cm<sup>2</sup>) and a ring electrode (Pt electrode, area 0.1866 cm<sup>2</sup>). The scanning rate of disk electrode was 5 mV s<sup>-1</sup> vs RHE and the ring electrode potential was 1.3 V vs RHE.

The electron transfer number ( $n$ ) and the hydrogen peroxide yield (%H<sub>2</sub>O<sub>2</sub>) were calculated according to the following equation: [11]

$$n = \frac{i_d}{i_d + i_r/N} \quad (1)$$

$$\text{H}_2\text{O}_2 (\%) = 200 \frac{i_r/N}{i_d + i_r/N} \times 100\% \quad (2)$$

Where  $i_d$  and  $i_r$  are the disk and ring currents, respectively.  $N$  is the ring collection efficiency ( $\sim 37\%$ ). The electron-transfer number ( $n$ ) of NSPC at different potentials was calculated according to the Koutecky-Levich equation.

$$1/j_d = 1/j_k + 1/B\omega^{1/2} \quad (3)$$

$$B = 0.2nFC_0(D_0)^{2/3}\nu^{-1/6} \quad (4)$$

where  $j_d$  and  $j_k$  are the kinetic- and diffusion-limited current densities of ORR;  $B$  is the theoretical value of the Levich slope  $B$  and can be calculated via equation of (1).  $n$  is the overall number of electrons transferred during the ORR,  $F$  is the Faraday constant,  $C_0$  is the bulk concentration of oxygen,  $D_0$  is the molecular diffusion coefficient of oxygen.  $\nu$  is the kinematic viscosity of the electrolyte. The coefficient 0.2 is adopted when the rotating speed is expressed in rpm. (In 0.1 M

KOH,  $C_0 = 1.2 \times 10^3$  mol L<sup>-1</sup>,  $D_0 = 1.9 \times 10^{-5}$  cm<sup>2</sup> s<sup>-1</sup>,  $\nu = 0.01$  cm<sup>2</sup> s<sup>-1</sup>. In 0.1 M HClO<sub>4</sub>,  $C_0 = 1.6 \times 10^3$  mol L<sup>-1</sup>,  $D_0 = 1.1 \times 10^{-5}$  cm<sup>2</sup> s<sup>-1</sup>,  $\nu = 0.01$  cm<sup>2</sup> s<sup>-1</sup>).

For Zn-air battery, the ORR air electrode (cathode) was prepared by uniformly depositing the as-prepared catalyst ink (20% Pt/C or NSPC) onto a carbon paper electrode (catalyst loading 0.5 mg cm<sup>-2</sup>), while a Zn plate was used as an anode. Both electrodes were assembled in a home-made Zn-air battery, and 6 M KOH was used as an electrolyte (Fig. S22). The discharge stability was tested on an electrochemical station (Land-CT2001 A, Wuhan, China) through galvanostatic discharge with different current densities, such as 5, 10, 20 and 25 mA cm<sup>-2</sup>. The polarization curve was also measured on an electrochemical station.

### 3. Results and discussion

#### 3.1. Preparation of protein hydrogel with tunable structures

BSA is a water-soluble globulin protein (pI, 4.7) in neutral aqueous solutions. It can assemble into protein fibers and further undergo a sol-to-gel transition to form protein hydrogels under alkaline condition (inset in Fig. 1b). Fig. 1b shows the dynamic frequency sweep of the hydrogels. The storage modulus ( $G'$ ) is always larger than the loss modulus ( $G''$ ) through the entire sweeping process, suggesting the formation of 3D hydrogel networks. The network structures are further validated by SEM (Fig. 1c & d) and TEM (Fig. 1e). A closer observation shows that there are some hexagonal crystals (mainly NaOH) within protein networks (Fig. 1d). Clearly, BSA can self-assemble into intertwined fibers, leaving porous structures within them. The hydrogel networks can be tuned by changing the mass ratio of NaOH to BSA. Specifically, BSA powders alone are with lamellar structure and smooth surface (Fig. S1). While, upon elevating the mass ratio of NaOH to BSA to 0.05, BSA can assemble into ‘lamellate array’ with compact structures (Fig. S2). The morphology change of protein hydrogel is

often related to the structural variation of protein molecules. The secondary structure of the protein molecules and assembling structures are highly related to chemical surroundings (e.g., pH), which can be reflected from the circular dichroism (CD) and UV-vis spectra. As depicted in the CD patterns in Fig. 1f, the absorbance of BSA at 208 and 222 nm gradually vanished at an evaluated ratio of NaOH to BSA, ascribed to the absorbance of  $\alpha$ -helix of BSA. The absorbance change indicates the transformation of BSA structure from  $\alpha$ -helix to random configuration [48]. When pH value of the medium is higher than pI of BSA (4.7), the BSA chains are negatively charged and can repulse mutually, leading to the unfolding of the  $\alpha$ -helical structure [49]. Fig. 1g represents the UV-vis absorbance changes of BSA aqueous. Absorbance at  $\sim 280$  and  $\sim 230$  nm can be ascribed to the  $n \rightarrow \pi^*$  transition of tryptophan and tyrosine residues and  $\pi \rightarrow \pi^*$  transition of  $C=O$  respectively, which is highly sensitive to protein configuration [49,50]. In addition, there is a redshift in absorbance upon increase of the ratio of NaOH to BSA, possibly due to the deprotonation of  $-NH=CO-$  and  $-OH$  in tryptophan and tyrosine residues, which is often accompanied by the aggregation of protein molecules. Meanwhile, the absorbance at 230 nm increases gradually with the increase of the ratio of NaOH to BSA, due to the scattering effects of the colloidal protein assemblies. Therefore, the difference in the morphology of hydrogel networks is possibly caused by the changes of secondary structure and assembling behavior of BSA molecules. Though the detailed information on how proteins change their structures under alkaline condition is still unclear, it is certain that the protein structure can be tuned via tuning the ratio of NaOH to BSA. The stimuli-response features of the protein hydrogel networks render them a structure-tunable precursor for fabricating functional carbon materials.

### 3.2. Influences of precursors and pyrolysis temperature on the pore structure of NSPC

N, S-codoped porous carbon (NSPC) materials were prepared by pyrolysis of BSA aerogels which were gained through freeze-drying protein hydrogels (Fig. 2a). The as-obtained NSPC materials are denoted as NSPC-x-y, where x and y indicate the mass ratio of NaOH to BSA and the pyrolysis temperature, respectively. As the above-mentioned, the composition and structure of the protein hydrogels, as a latent precursor, are determined by NaOH content. Therefore, the ratio of NaOH to BSA can be explored for describing the structure and composition of precursors. As shown in Fig. 2c and Fig. S3 & 4, NSPC shows plate-like structures. By contrast, NSPC-0.2-900 is relatively thinner and well dispersed in aqueous solution after sonication, and displays typical *Tyndall Effect* (Inset in Fig. 2b). Intriguingly, a closer observation shows that there are some pores with sizes ranging from  $\sim 1$  nm to dozens of nanometers for NSPC-0.2-900 (Fig. 2d & 2e). The high resolution-TEM (HR-TEM) image reveals that NSPC-0.2-900 is highly graphitized. The lattice spacing ( $\sim 0.35$  nm) indexed to the (002) of graphite carbon can be seen (Fig. 2f). However, it is slightly larger than that of perfect graphite structure (0.335 nm), demonstrating the existence of a turbostratic structures in NSPC-0.2-900 [51]. TEM images and corresponding electron energy-loss spectroscopy (EELS) mapping images of NSPC-0.2-900 demonstrate the coexistence of C, N, S and O in the NSPC structure (Fig. 2g & 2h). Heteroatom (N, S) dopant can promote the adsorption and polarization of  $O_2$  on the surface of carbon and thus increase the activity of ORR [11,52]. Typical carbon K-edge spectrum of NSPC-0.2-900 is illustrated in Fig. 2i. It displays well-defined peaks at around 285.8 and 293.1 eV attributed to electron transitions from the 1 s to the  $\pi^*$  state and 1 s to  $\sigma^*$  state respectively, which suggests that the carbon atom is in the  $sp^2$  hybridization state. Particularly, the sharp  $\pi^*$  peaks demonstrate that NSPC-0.2-900 has a high  $sp^2$ -C ratio, in good agreement with the HR-TEM results [53,54].

To investigate the influences of precursor on the porous structures of NSPC, the  $N_2$  adsorption-desorption isotherms and corresponding pore size distribution of NSPC were gained. As illustrated in Fig. 3a &

3b, the adsorption pore volume and specific surface area follow the order of NSPC-0-900 ( $378.7\text{ m}^2\text{ g}^{-1}$ )  $<$  NSPC-0.05-900 ( $619.9\text{ m}^2\text{ g}^{-1}$ )  $<$  NSPC-0.2-900 ( $1274\text{ m}^2\text{ g}^{-1}$ ). Clearly, the precursors formed under a higher ratio of NaOH to BSA, favor the generation of carbon materials with larger adsorption volume and specific surface area. In contrast, NSPC-0-900 possesses typical type I adsorption isotherm. The adsorption capacity shows a remarkable increase at low pressure and arrives at a plateau rapidly, which indicates the existence of micropore within NSPC-0-900. NSPC-0.05-900 exhibits a mixed type I and IV (featuring a visible H3 hysteresis loop) adsorption-desorption isotherms, suggesting the coexistence of micropore and mesopore. By contrast, NSPC-0.2-900 displays a mixed type I, II and small degrees of IV adsorption-desorption isotherms, indicating that NSPC-0.2-900 possesses hierarchically porous structures. The pore structure is verified by the pore size distribution. In detail, NSPC-0-900 possesses micropore while NSPC-0.05-900 has both micropore and mesopore, and NSPC-0.2-900 owns collective porous structures of micropore, mesopore and macropore.

The influence of pyrolysis temperature on the porous structures of NSPC was also investigated. As shown in Fig. 3c, both the adsorption volume and specific surface area undergo a remarkable increase with an increased pyrolysis temperature. The specific surface area of NSPC-0.2-900 ( $1274\text{ m}^2\text{ g}^{-1}$ ) is twice and 70 times larger than that of NSPC-0.2-700 ( $548.7\text{ m}^2\text{ g}^{-1}$ ) and NSPC-0.2-500 ( $17.36\text{ m}^2\text{ g}^{-1}$ ) respectively. The pyrolysis temperature can also affect the porous structure and the isotherm curve of the obtained carbon materials. As shown in Fig. 3c, NSPC-0.2-700 exhibits a mixed isotherm curve of type I and II, while NSPC-0.2-500 features only II isotherm curve, which implies that micropore and macropore coexisted within NSPC-0.2-700 and only macropore for NSPC-0.2-500. This agrees well with the pore size distribution curve, where a bimodal pore size distribution was found for NSPC-0.2-700, centered at around 0.6 to 2 nm and 50 to 100 nm respectively. In comparison, only single modal porous structure was found for NSPC-0.2-500 at around 50–100 nm (Fig. 3d). Accumulated pore volumes for different samples were summarized in Fig. 3e. Overall, the single-point total pore volume follows the order of NSPC-0-900 ( $0.1968\text{ cm}^3\text{ g}^{-1}$ )  $<$  NSPC-0.05-900 ( $0.3296\text{ cm}^3\text{ g}^{-1}$ )  $<$  NSPC-0.2-900 ( $0.8552\text{ cm}^3\text{ g}^{-1}$ ). Obviously, porous structure can be tuned by precursors or/and carbonization temperature. In general, several factors can lead to forming different types of porous structures: (i) The protein hydrogel networks intrinsically possess numerous pores. (ii) A large amount of gaseous species, such as  $H_2O$ ,  $CO_2$ ,  $SO_2$  and  $NO_2$  are generated during the pyrolysis process. These generated gases evaporate and leave more pores especially micropore in NSPC. (iii) The homogeneously embedded NaOH in the precursor can etch the carbon structure to further generate pores [55,56]. Thus, the influence of precursors and pyrolysis temperature on the pore structure can be illustrated as follows. Higher ratio of NaOH to BSA makes precursors with loosen structures, which possibly leads to carbon structure with more pores after carbonization. Meanwhile, the excessive alkali can not only help to produce micropore but also continuously etch micropore into mesopore or macropore. Therefore, higher ratio of NaOH to BSA can produce larger pore volumes and drive the transition of porous structure from single micropore to mixed mesopore and even macropore. Besides, at relative low pyrolysis temperature, proteins cannot be carbonized completely. As a result, fewer pores are generated when the pyrolysis temperature declined from  $900^\circ C$  to  $500^\circ C$ .

The presence of porous structures is often accompanied with the existence of the defected carbon structures. As shown in Fig. 3f, NSPC obtained under high temperature displays two peaks at around  $25^\circ$  and  $43^\circ$  assigned to the (002) and (100) of graphitic carbon respectively. Compared to NSPC-0-900, NSPC-0.05-900 and NSPC-0.2-900 show smaller  $2\theta$  with a broader peak, suggesting the higher degree of disorder. The defected structures of NSPC were further evaluated by Raman spectra. As shown in Fig. 3g, there are two peaks at around  $1350$  and  $1580\text{ cm}^{-1}$  for all NSPC samples, assigned to D band and G band of

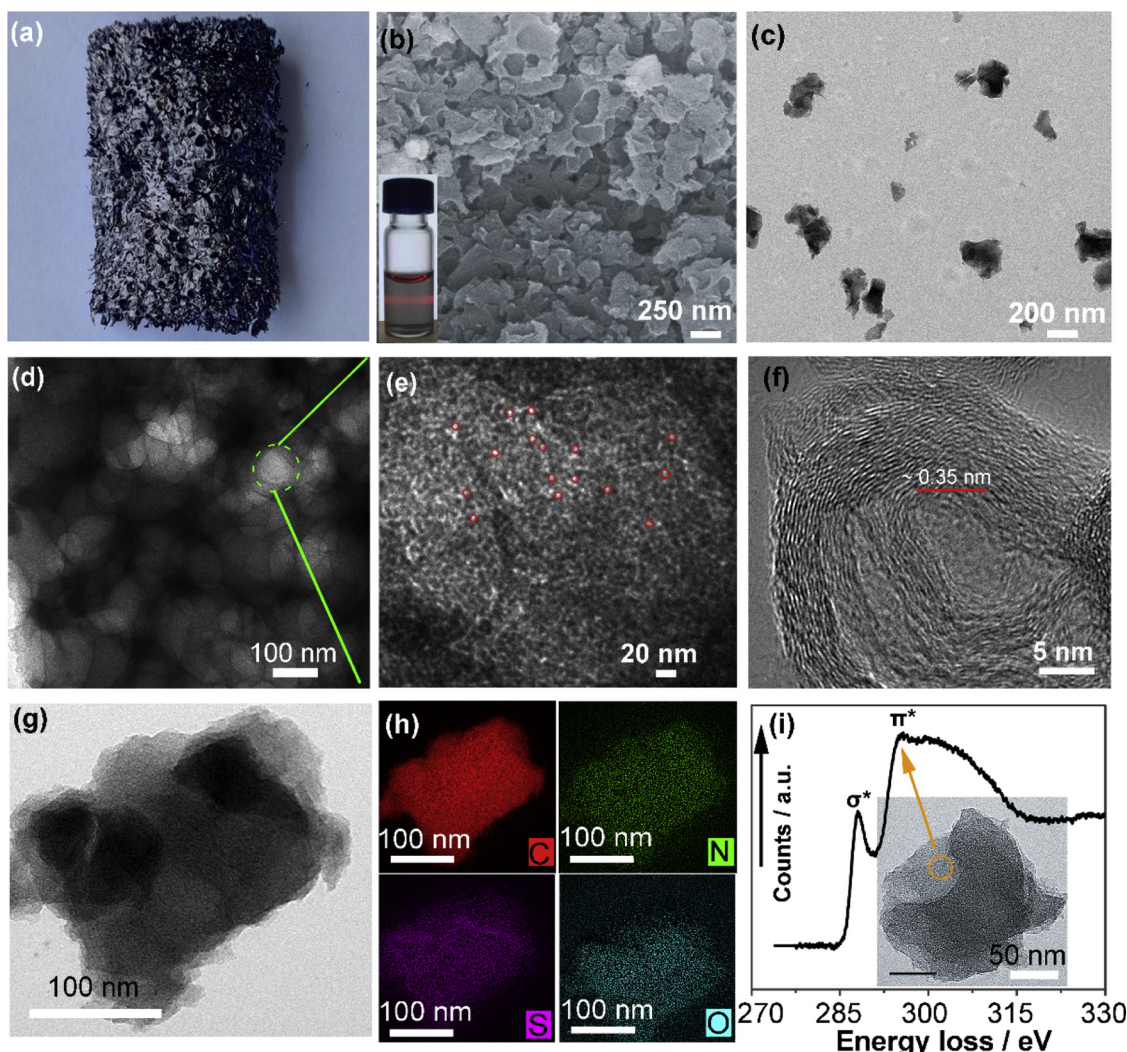


**Fig. 2.** (a) Typical photograph of NSPC. (b–i) Characterization of NSPC-0.2-900: (b) SEM image, (c–e) TEM images, (f) HR-TEM image, (g) TEM image and corresponding (h) C,N,S,O energy-filtered TEM images and (i) typical carbon K-edge EELS spectra of selected areas (inset in (i) marked in yellow) of NSPC-0.2–900 (For interpretation of the references to colour in this figure legend, the reader is referred to the web version of this article).

graphite carbon respectively [26,57]. The  $I_D/I_G$  for different samples follows the order of NSPC-0.2-900 > NSPC-0.05-900 > NSPC-0-900. The XRD and Raman results reveal that structural defects occur along with the presence of porous structure. Generally, heteroatom-doped carbon can work as Lewis base sites for ORR. Both porous and defected structure can affect the  $O_2$  adsorption on the surface of carbon materials. Herein,  $CO_2$  was chosen as a probe to examine the influences of porous structure on the Lewis base sites. As shown in Fig. 3h, hierarchically porous NSPC-0.2-900 with the largest pore volume exhibits a higher adsorption capacity of  $CO_2$  compared to that of NSPC-0-900 and NSPC-0.5-900. This demonstrates that the porous structure allows more active site to be exposed, which is beneficial for the catalysis of ORR (Fig. 3i).

### 3.3. Influences of the precursors and pyrolysis temperature on the composition of NSPC

To study the influences of precursor and pyrolysis temperature on the composition of carbon materials, X-ray photoelectron spectroscopy (XPS) measurement was carried out. As shown in Fig. S5 and Table S1, the characteristic peaks of C, N, S and O are found in the XPS patterns for all NSPC samples, indicating the successful dopant of N and S. Fig. 4a and Fig. S6–9 present the N 1 s XPS patterns of NSPC. Generally,

the N 1 s of all NSPC samples can be fitted into four-form, content-different N species. For example, NSPC-0.2-900 possesses pyridinic N (398.2 eV, 32.1%), pyrrolic N (399.9 eV, 26.7%), graphitic N (401.1 eV, 30.8%) and oxidized N (403.2 eV, 10.4%) (Fig. 4a). Generally, compared with C atom, N possesses higher electronegativity, enabling the charge transfer from the nitrogen atom to the adjacent carbon atom, which results in the chemisorption of  $O_2$  and readily attracting electrons from the anode for the ORR [11]. This is particular the case for pyrrolic N and graphitic N, since graphitic N can enhance the electrocatalytic activity of the carbon while pyridinic-N is beneficial for the electron transfer and decrease the overpotential for ORR. Thus, pyrrolic N and graphitic N are generally believed to be the catalytic center for ORR in both basic and acidic conditions [11,52,53,58].

It is found that both pyrolysis temperature and types of precursors can influence the content of the N species. Both the total N content and total percentage of pyridinic N plus graphitic N decrease at an elevated temperature from 500 °C to 900 °C (Fig. 4c, b). Besides, we found that precursors with a higher NaOH ratio can lead to a higher percentage of pyrrolic N and oxidized N. The influences of pyrolysis temperature and precursors on the composition of carbon structure can be explained as follows. Under higher pyrolysis temperature, N element is readily oxidized into gaseous compounds, such as  $NO_x$ , thus less amount of N is left [59]. Meanwhile, carbon atoms adjacent to pyridinic or graphitic

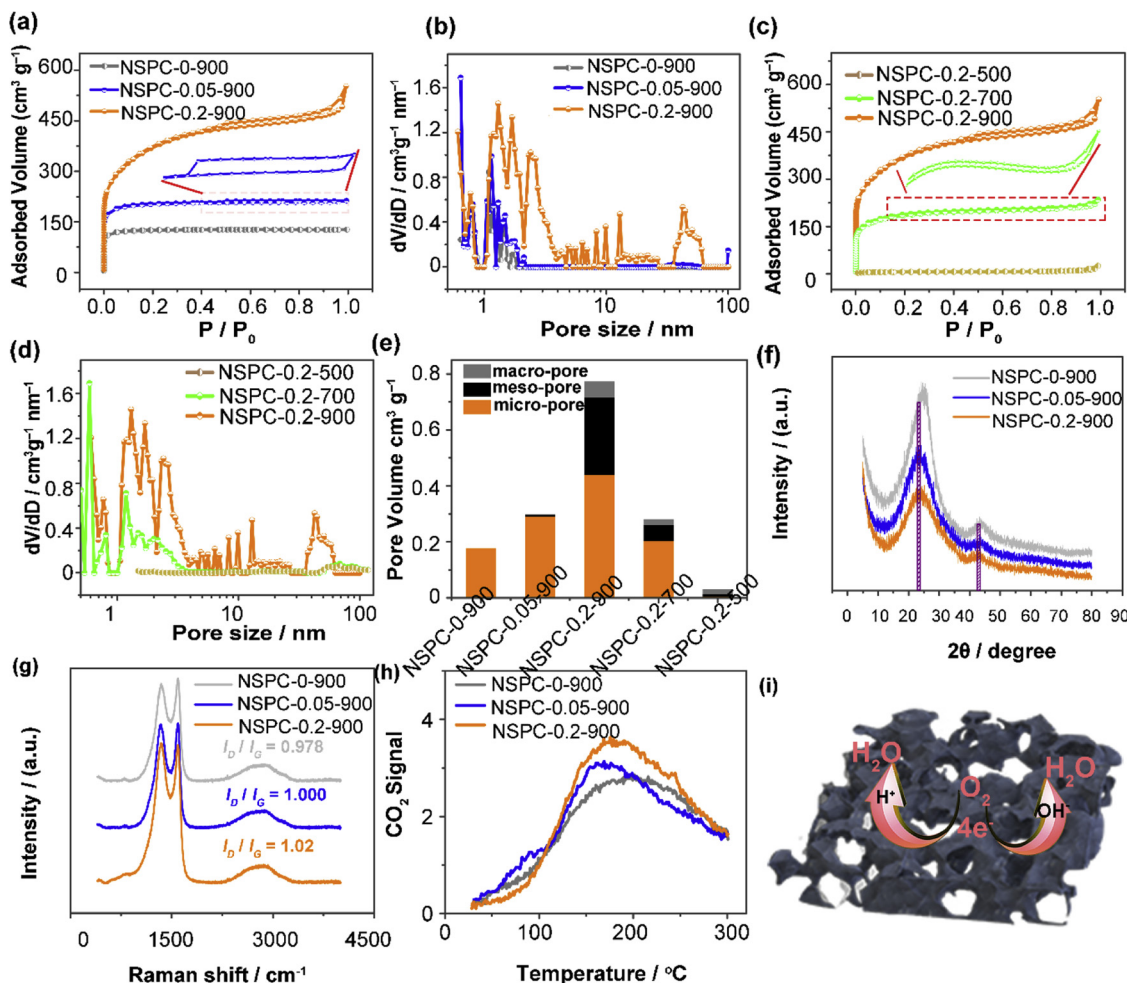


**Fig. 3.** Structural characterization and properties of NSPC materials. (a & c) N<sub>2</sub> adsorption isotherms and (b & d) pore size distribution of NSPC respectively: (a & b) obtained from different precursors formed under different ratios of BSA to NaOH, (c & d) obtained from different pyrolysis temperature. (e) Collective pore volumes of different NSPC. (f) XRD spectra, (g) Raman patterns, (h) CO<sub>2</sub>-TPD measurement of NSPC obtained from different precursors. (i) Schematic illustration of ORR activities in both acidic and alkaline conditions of hierarchically porous NSPC-0.2-900.

nitrogen show strong nucleophilic affinity, and are apt to suffer the nucleophilic attack, which is aggravated by raising the pyrolysis temperature [55,60]. Therefore, the thermodynamically stable pyrrolic N can be increased by raising the pyrolysis temperature and content of OH<sup>-</sup>. While, the nucleophilic attack can lead to the breakup of the original planar structure and result in more porous and defected carbon structures, in consistent with the experimental results that more pores can be generated under higher pyrolysis temperature and NaOH content.

The high-resolution XPS spectra of S 2p were also analyzed. The S 2p peaks are centered at around 164.5, 165.5, 167.9, and 170.2 eV (Fig. 4b and Fig. S6-9). The former two can be assigned to S 2p<sub>3/2</sub> and S 2p<sub>1/2</sub> of thiophene ( $-C-S-C-$ ), respectively, while the peaks at 167.9 and 169.3 eV are attributed to oxidized-S groups ( $-C-SO_x-C-$ ) [18,61,62]. Though all NSPC samples possess relative low S content (< 0.6%) (Fig. 4d), S plays a crucial role in determining the ORR capacity of the carbon materials especially in acid [42]. Sulfur prefers to induce topological defects once inserted into carbon structures, which is beneficial for the production of active sites and their exposure. The S content shows an obvious decrease upon raising the ratio of NaOH to BSA or pyrolysis temperature. Meanwhile, higher pyrolysis temperature leads to larger percentages of thiophene-S, which possesses higher ORR activity than the oxidized-S does. To sum up, even after high pyrolysis temperature, there are still certain amounts of heteroatom (i.e., N, S) left within the carbon structure. And more importantly, the

consumption of heteroatoms can be accompanied by the occurrence of porous and defected structures, which is able to enhance the availability of active sites and thus beneficial for the ORR process. Of particular, Lewis base sites within carbon structure are often regarded as the active centers for ORR. The CO<sub>2</sub>-TPD results exhibit that NSPCs-0.2-900 has a larger adsorption volume of CO<sub>2</sub> compared to NSPC-0-900 and NSPC-0.05-900, though they have similar N, S contents.

#### 3.4. Electrocatalytic activity of NSPC in alkaline condition

The electrocatalytic performance of the as-obtained carbon materials with different porous structures were evaluated in a three-electrode system in an O<sub>2</sub>-saturated electrolyte. Firstly, cyclic voltammetry (CV) was performed in an O<sub>2</sub> or N<sub>2</sub>-saturated KOH solution (0.1 M) with Pt/C (20 wt% Pt, Johnson Matthey) as a reference catalyst. As shown in Fig. S10, all NSPC samples exhibit oxygen reduction peaks in O<sub>2</sub>-saturated KOH solution but not in N<sub>2</sub>-saturated ones. The reduction potential (vs. RHE) follows the order of NSPC-0.2-500 < NSPC-0-900 < NSPC-0.2-700 ~ NSPC-0.05-900 < NSPC-0.2-900, the same order to that of pore volume, which indicates that pore structure plays a crucial role in ORR. Hierarchically porous NSPC-0.2-900 performs best among all NSPC samples. The reduction potential of NSPC-0.2-900 is around 0.81 V, comparable to that of Pt/C. Liner sweep voltammetry (LSV) measurements were performed to further investigate the ORR activity of NSPC. As shown in Fig. 5a and Fig. S11–S14, NSPC-0.2-900

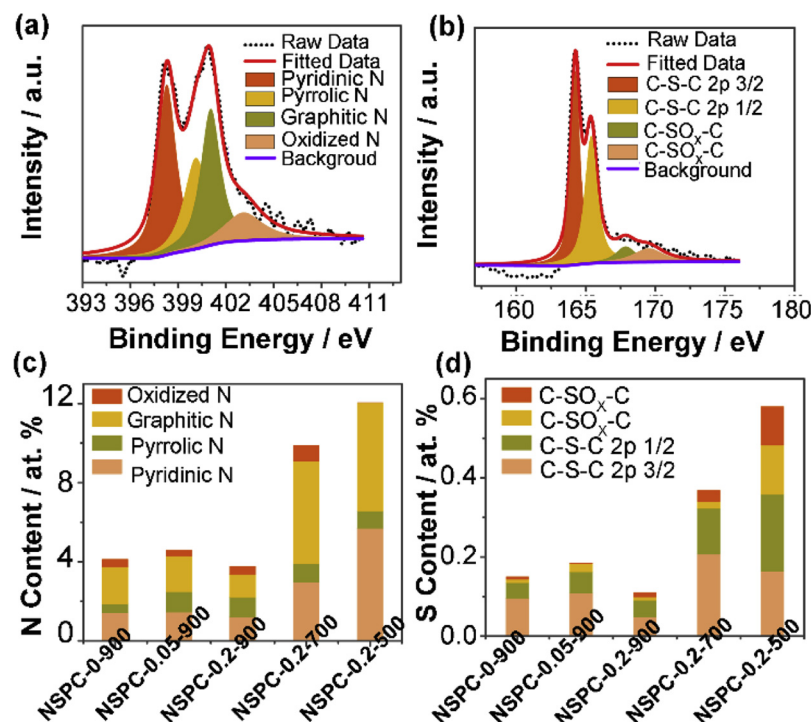


Fig. 4. (a) N 1 s and (b) S 2p spectra of NSPC. (c) The contents of four nitrogen species in NSPC. (d) The contents of four sulfur species in NSPC.

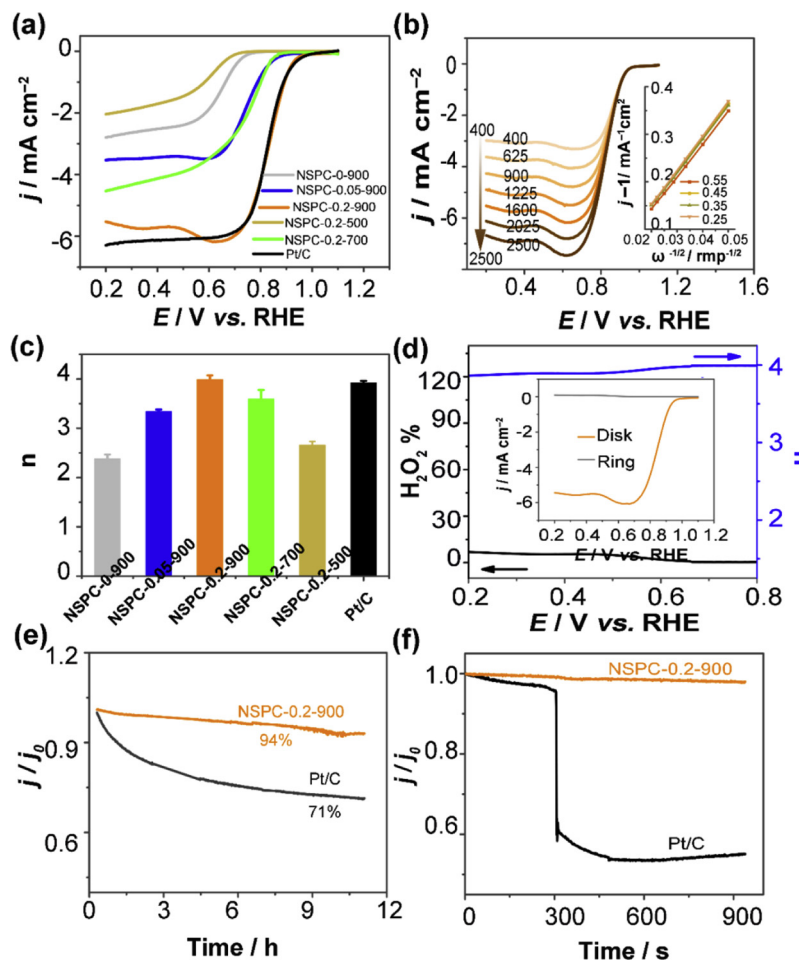


Fig. 5. ORR properties of NSPC in 0.1 M KOH. (a) LSV curves of NSPC and Pt/C at a rotation rate of 1600 rpm and a scan rate of 5 mV/s. (b) LSV curves of NSPC-0.2-900 under the rotation rate from 400 to 2500 rpm at a scan rate of 5 mV/s. The inset presents the corresponding K-L plot. (c) The electron transfer number (*n*) for NSPC calculated from the K-L curves. (d) H<sub>2</sub>O<sub>2</sub> yield and the calculated *n* of NSPC-0.2-900, and the inset in (d) presents the RRDE voltammograms. (e) Catalytic stability of NCPC-0.2-900 and Pt/C 0.1 M KOH electrolyte for 30,000 s at 0.65 V. (f) Chronoamperometric response of NCPC-0.2-900 and Pt/C before and after the addition of 500  $\mu$ L of methanol to 150 mL of O<sub>2</sub>-saturated 0.1 M KOH at 0.71 (vs. RHE).

displays a more positive onset potential ( $E_{\text{onset}}$ , ~0.93 vs. RHE), half-wave potential ( $E_{1/2}$ , ~0.83–0.84 V vs. RHE) and diffusion-limit current density ( $j$ , 5.8 mA cm<sup>-2</sup>), which is comparable with that of Pt/C ( $E_{\text{onset}}$ , ~0.94 V vs. RHE;  $E_{1/2}$ , ~0.82–0.83 vs. RHE;  $j$ , ~6.18 mA cm<sup>-2</sup>). Like most porous carbon-based ORR electrocatalysts, the LSV curves of NSPC show slight fluctuation [13,63]. Unlike traditionally precious metal catalysts (e.g., Pt), there exist the issue of distribution of active sites within porous carbon. For Pt catalysts, O<sub>2</sub> reduction process is fast and mainly happens on the outer part of Pt, thus a flat limiting platform can be obtained. While for carbon-based catalysts, the active sites exist within the porous carbon, it is difficult to achieve pure diffusion-limited conditions. Meanwhile, the O<sub>2</sub> penetration inside the active sites and O<sub>2</sub> reduction rate depend on the exerted potential, which is related to the current density. As a result, the LSV curves often exhibit fluctuation for porous carbon based ORR catalysts [64–66]. Clearly, pore structure can exert great influences on the ORR activity. Overall, larger pore volume can help to expose more active sites. Although NSPC-0.2-900 has low total N contents and S content, it possesses larger pore volume than other samples do, which means more active sites are exposed. When the ratio is higher than 0.2, (e.g. 0.25), the obtained NSPC-0.25-900 presents a reduced ORR capacity in both acid and basic conditions (Fig. S15). As mentioned above, high NaOH ratio is beneficial for etching the carbon into porous structure, which is beneficial for the exposure of active sites. However, further increasing the NaOH amount, the pore volume, especially the mesopore volume declined remarkably, resulting in a lowered ORR activity of the catalyst (Fig. S15). In addition, too high ratio of NaOH can lead to the mass loss of the carbon materials. In addition, compared to mesopore or macropore, micropore (of similar pore volume) can expose more active sites and exert a more distinctive confinement effect. This can help to explain why NSPC-0.05-900 performs slightly better than NSPC-0.2-700 whose micropore content is lower than the former ones. Of note, the unique porous structure affords NSPC-0.2-900 excellent ORR activity, which outperforms most metal-free catalysts (Table S2). The electron transfer number ( $n$ ) calculated from Koutecky-Levich (K-L) curves was used to evaluate the ORR activity of NSPC. As shown in Fig. 5b, we can observe well-defined platforms of diffusion-limiting currents, which show a gradually increase upon the raising rotation rate from 400 to 2500 rpm. A good linearity of K-L curves ( $J^{-1}$  vs.  $\omega^{-1/2}$ ) was obtained (inset in Fig. 5b). The  $n$  calculated from K-L curves for each sample is shown in Fig. 5c, where  $n$  varies from 2.4 to 4 for different NSPC samples. Among these samples, hierarchically porous NSPC-0.2-900 has a similar  $n$  value to that of Pt/C (3.99 vs. 3.92), implying a 4e<sup>-</sup> ORR pathway in alkaline medium. The  $n$  value for NSPC-0.2-700 (3.6) is a bit larger than that for NSPC-0.05-900 (3.4), while the  $n$  value for both of them are larger than that for NSPC-0.900 (~2.4) and NSPC-0.2-700 (2.6). Though NSPC-0.2-700 and NSPC-0.05-900 have similar pore volume, there are a certain number of mesopore in NSPC-0.2-700, which is beneficial for the rapid mass transfer of both water and O<sub>2</sub> and thus favor a reduction of O<sub>2</sub> in a 4e<sup>-</sup> pathway.

To further evaluate the ORR pathways for NSPC-0.2-900, rotating ring-disk electrode (RRDE) measurements were performed. As shown in Fig. 5d (inset), NSPC-0.2-900 exhibits high disk current density (~5.6 mA cm<sup>-2</sup>) and much lower ring current density (~0.06 mA cm<sup>-2</sup>) which are generated from O<sub>2</sub> reduction and hydrogen peroxide oxidation respectively. Fig. 5d describes the corresponding  $n$  and the amount of the generated H<sub>2</sub>O<sub>2</sub> from RRDE curves. It can be seen that NSPC-0.2-900 undergoes a nearly 4e<sup>-</sup> ORR pathway and is quite efficient with only a small amount of peroxides species were generated (less than 8%). Subsequently, the catalytic stability of NSPC-0.2-900 was tested by chronoamperometric response measurement. Nearly 94% current retention is achieved for NSPC-0.2-900 even after 12 h, much higher than that of Pt/C (71%) (Fig. 5e). This was further confirmed by CV test. After cycling for 10,000 times, the CV curves overlap well for NSPC-0.2-900 before and after test, while an obvious loss of  $J$  and  $E$  (reduction peak potential) was obtained for Pt/C (20%) (Fig. S16). This

agrees well with that XPS results, which were performed after 10,000 cycles. As illustrated in XPS spectra, there exists only slight fluctuation with respect to the main active sites that are pyridinic- and graphitic-N. Besides, no obvious changes were obtained for S species (Fig. S17 and Table S3). The methanol crossover effects for NSPC-0.2-900 and Pt/C were also investigated respectively. As shown in Fig. 5f, the introduction of methanol into electrolyte causes a distinctive currency response for Pt/C. By contrast, only negligible changes are observed for NSPC-0.2-900 under paralleled conditions.

### 3.5. Electrocatalytic activity of NSPC in acidic condition

Metal-free catalysts often have poor ORR catalytic activity in acidic medium, possibly owing to the inactivation of active sites that are originally efficient in alkaline condition. This is particularly the case for N-doped carbon structures. However, most metal-free catalysts show much poorer ORR performance in acidic condition than that in basic condition. Carbon-based catalysts often undergo an inefficient two-electron ORR in acidic condition, and produce undesired byproducts, e.g., H<sub>2</sub>O<sub>2</sub>, which can possibly corrode the active sites. In addition, N atom tends to be protonated in acidic condition, followed by absorption of anions, damaging the ORR active sites [67]. It was found the introduction of S into the carbon structures can create structural defects and new active sites that are rather robust and effective for ORR in acidic medium [41]. More importantly, the presence of hierarchical pores could not only raise the local concentration of O<sub>2</sub> but also allow more active sites to be approached by O<sub>2</sub>. Therefore, NSPC samples possibly possess an enhanced ORR activity in acidic condition. Thus, the ORR activity of NSPC in acidic medium was evaluated. Fig. S18 depicts the CV curves of NSPC in O<sub>2</sub> or N<sub>2</sub> saturated HClO<sub>4</sub> (0.1 M). NSPC-0.2-900 possesses a more positive reduction potential than other samples do. This agrees well with the LSV tests, where NSPC-0.2-900 owns more positive onset potential ( $E_{\text{onset}}$ , ~0.81 V vs RHE), half-wave potential ( $E_{1/2}$ , ~0.71 V vs RHE) and larger limited current density ( $j$ , ~5.60 mA cm<sup>-2</sup>) than that of other samples (Fig. 6a). Although the onset and half-wave potential are slightly less than that of Pt/C ( $E_{\text{onset}}$ , ~0.89 V;  $E_{1/2}$ , ~0.79 V) respectively, their catalytic property is much better than most of the reported carbon materials (Table S4). Similarly, porous structure in NSPC plays an important role in ORR performance in acidic medium. Compared with hierarchically porous NSPC-0.2-900, the other NSPC samples exhibit much smaller pore volume and are only with single modal porous structures, implying a significant loss in active sites. Meanwhile, both the confinement effects from micropores and mass transfer from mesopores are weakened. For example, only a neglected electrochemical response is observed for NSPC-0.2-500 and NSPC-0.900, as both of which have small pore volume. LSV curves for different samples are shown in Fig. 6b and Fig. S19 & 20. The average  $n$  of NSPC-0.2-900 obtained via K-L curve is 3.86, suggesting a 4e<sup>-</sup> ORR pathway in HClO<sub>4</sub> (0.1 M). By contrast, the  $n$  value of NSPC-0.2-700 and NSPC-0.05-900 are 3.3 and 2.7, respectively, indicating that they implement a mixed two-electron and four-electron process (Fig. 6c). The 4e<sup>-</sup> ORR pathway of NSPC-0.2-900 is further validated by the RRED measurement, where the  $n$  values range from 3.7 to 3.9 within a potential range of 0.2 to 0.8 V. Furthermore, the peroxide yield is quite low within a wide operation potential range, which demonstrates that NSPC-0.2-900 is of high O<sub>2</sub> reduction selectivity in acidic medium (Fig. 6d). In addition, NSPC-0.2-900 shows high stability and robustness towards methanol crossover effect (Fig. 6e, Fig. S21 and Fig. 6f). Such an excellent electrocatalytic activity of NSPC-0.2-900 enables it a potential candidate for fabricating polyelectrolyte membrane (PEM) fuel cells. The results suggest that hierarchically porous structures are beneficial for ORR in acidic condition, owing to their synergistic effects of different types of pore structures on enhancing the active sites and promoting mass transfer.

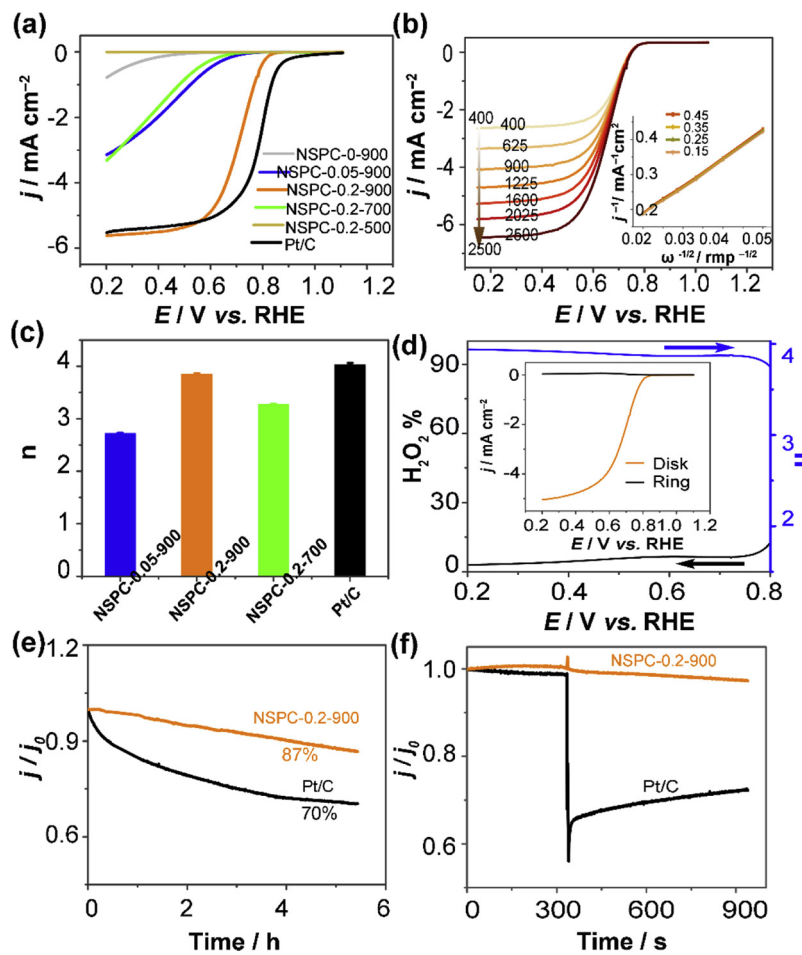


**Fig. 6.** ORR properties of NSPC in 0.1 M  $HClO_4$ . (a) LSV curves of NSPC and Pt/C at a rotation rate of 1600 rpm and a scan rate of 5 mV/s. (b) LSV curves of NSPC-0.2-900 under the rotation rates from 400 to 2500 rpm at a scan rate of 5 mV/s. The inset presents the corresponding K-L plot. (c) The electron transfer number ( $n$ ) for NSPC calculated from the K-L curves. (d)  $H_2O_2$  yields and the  $n$  of NSPC-0.2-900 and the inset in (d) presents the RRDE voltammograms. (e) Catalytic stability of NCPC-0.2-900 and Pt/C 0.1 M KOH electrolyte for 20 000 s at 0.62 V vs. RHE (f) Chronoamperometric response of NCPCSS-0.2-900 and Pt/C before and after addition of 0.5 mL of methanol to 150 mL of 0.1 M  $O_2$ -saturated 0.1 M  $HClO_4$  at 0.62 V vs. RHE.

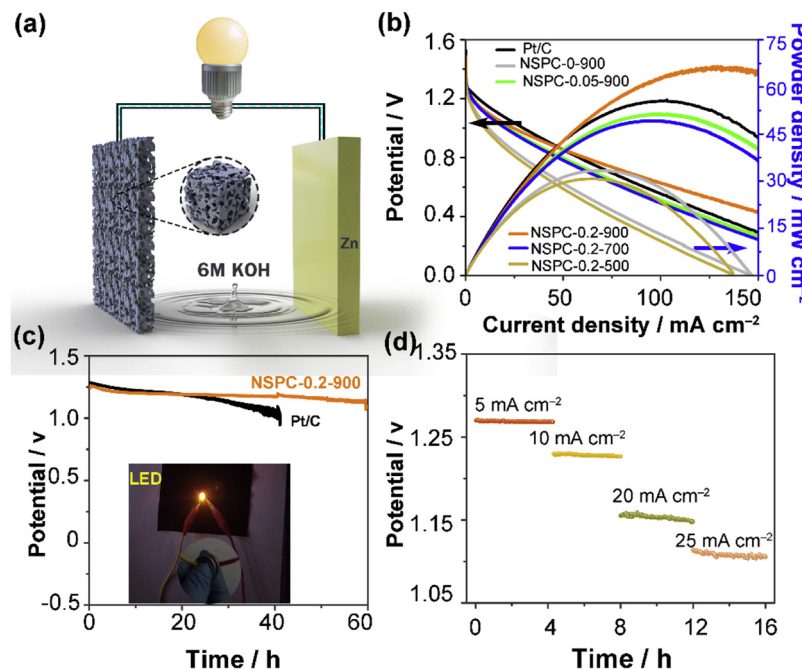


**Fig. 7.** (a) Schematic representation for the primary ZABs. (b) Polarization and power density curves of primary ZABs using NSPC and Pt/C as the ORR electrocatalyst, respectively. (c) Long-term galvanostatic discharge curves of primary ZABs with NSPC-0.2-900 and Pt/C as cathode catalysts, respectively. The inset presents the optical images of LED light powered by two ZABs in series. (d) Galvanostatic discharge plots with NSPC-0.2-900 as an air-cathode at various current densities.

### 3.6. Performance of Zn-air batteries based on NSPC

A primary zinc-air battery (ZAB) was assembled to test the feasibility of NSPC in practical application (Fig. S2). In detail, NSPC-0.2-900 loaded on a carbon paper was utilized as an air cathode, Zn foil as an

anode, and 6 M KOH aqueous solution as electrolyte respectively (Fig. 7a). The electrochemical performance of ZAB was tested on a home-made two-electrode device. As depicted in Fig. 7b, NSPC-0.2-900 shows the highest power density, current density and open-circuit potential, which even exceed that of Pt/C electrode within a wide current

density range. The ZABs properties of NSPC are comparable and even superior to those equipped with biomass-derived materials as cathodic catalysts (Table S5). The superior performance of NSPC-0.2-900 possibly comes from its hierarchically porous structure, which affords NSPC-0.2-900 more active sites for ORR and allows adequate dispersion of O<sub>2</sub> and electrolyte to approach the active sites. NSPC-0.2-900 shows a highly stability and no potential drop is observed during the long-term discharging (60 h) (Fig. 7c). This is much better than Pt/C based air cathode. Galvanostatic discharge test shows that the potential plateau of NSPC-0.2-900 locate at 1.27, 1.23, 1.16, and 1.11 V for 5, 10, 20 and 25 mA cm<sup>-2</sup> discharge current densities, respectively (Fig. 7d). Also, only negligible potential drop was observed after discharging for 4 h, which can be ascribed to the exceptional stability of NSPC-0.2-900. NSPC-0.2-900 air-electrode was also assembled into diverse circuits to meet the specific power/energy requirements for practical applications. For example, they are proved able to illuminate a red light-emitting diode (LED, 2.89 V) (inset in Fig. 7c). A collection of the structure character of the obtained NSPC and their properties in ORR and ZABs were summarized in Table S6. In conclusion, the developed N, S-co-doped hierarchically porous carbon materials hold a great promise as electrocatalysts for fabricating diverse energy devices of practical applications.

#### 4. Conclusions

Proteins can self-assemble into hydrogel networks under alkaline condition. The networks can be tailed by changing the contents of alkali, which provides diverse precursors for fabricating heteroatom (N, S) self-doped carbon materials with tunable porous structures. Through regulating the precursor and/or pyrolysis temperature, the pore structure can be tuned from micropore to mixed micropore and mesopore structures, finally to hierarchical pores. The as-obtained hierarchically porous carbon material (NSPC-0.2-900) exhibits excellent ORR performance in both acidic and basic media, due to its heteroatom doping and hierarchically porous structures. In addition, using NSPC-0.2-900 as an air cathode catalyst, the gained ZAB shows a higher power density and better durability than Pt/C. This work provides a green, facile and cost-effective strategy for scalable synthesis of structure-tunable carbon materials, which can be utilized in various energy devices.

#### Acknowledgements

This work was supported by the National Natural Science Foundation of China (No. 21636010 and 21878342); the State Key Laboratory of Powder Metallurgy, Central South University, Changsha, China; the China Postdoctoral Science Foundation (No. 2018M64300); the Postdoctoral Science Foundation of Central South University (No. 205440) and Key Laboratory of Photochemical Conversion and Optoelectronic Materials (PCOM201816), TIPC, CAS, Beijing, China.

#### Appendix A. Supplementary data

Supplementary material related to this article can be found, in the online version, at doi:<https://doi.org/10.1016/j.apcatb.2019.01.050>.

#### References

- [1] I. Katsounaras, S. Cherevko, A.R. Zeradjanin, K.J. Mayrhofer, Oxygen electrochemistry as a cornerstone for sustainable energy conversion, *Angew. Chem. Int. Ed.* 53 (2014) 102–121.
- [2] Y. Li, H. Dai, Recent advances in zinc-air batteries, *Chem. Soc. Rev.* 43 (2014) 5257–5275.
- [3] M. Debe, Electrocatalyst approaches and challenges for automotive fuel cells, *Nature* 486 (2012) 43–51.
- [4] F. Cheng, J. Chen, Metal-air batteries: from oxygen reduction electrochemistry to cathode catalysts, *Chem. Soc. Rev.* 41 (2012) 2172–2192.
- [5] N. Komba, Q. Wei, G. Zhang, F. Rosei, S. Sun, Controlled synthesis of graphene via electrochemical route and its use as efficient metal-free catalyst for oxygen reduction, *Appl. Catal. B* 243 (2019) 373–380.
- [6] H.-F. Wang, C. Tang, Q. Zhang, A review of precious-metal-free bifunctional oxygen electrocatalysts: rational design and applications in Zn–air batteries, *Adv. Funct. Mater.* 28 (2018) 1803329.
- [7] J. Pan, Y. Xu, H. Yang, Z. Dong, H. Liu, B. Xia, Advanced architectures and relatives of air electrodes in Zn-air batteries, *Adv. Sci.* 5 (2018) 1700691.
- [8] X. Zheng, J. Wu, X. Cao, J. Abbott, C. Jin, H. Wang, P. Strasser, R. Yang, X. Chen, G. Wu, N., P., and S-doped graphene-like carbon catalysts derived from onium salts with enhanced oxygen chemisorption for Zn-air battery cathodes, *Appl. Catal. B* 241 (2019) 442–451.
- [9] P. Tan, B. Chen, H. Xu, W. Cai, W. He, M. Ni, In-situ growth of Co<sub>3</sub>O<sub>4</sub> nanowire-assembled clusters on nickel foam for aqueous rechargeable Zn-Co<sub>3</sub>O<sub>4</sub> and Zn-air batteries, *Appl. Catal. B* 241 (2019) 104–112.
- [10] W. Wan, X. Liu, H. Li, X. Peng, D. Xi, J. Luo, 3D carbon framework-supported CoNi nanoparticles as bifunctional oxygen electrocatalyst for rechargeable Zn-air batteries, *Appl. Catal. B* 240 (2019) 193–200.
- [11] K. Gong, F. Du, Z. Xia, M. Durstock, L. Dai, Nitrogen-doped carbon nanotube arrays with high electrocatalytic activity for oxygen reduction, *Science* 323 (2009) 760–764.
- [12] M. Zhou, H.-L. Wang, S. Guo, Towards high-efficiency nanoelectrocatalysts for oxygen reduction through engineering advanced carbon nanomaterials, *Chem. Soc. Rev.* 45 (2016) 1273–1307.
- [13] L. Dai, Y. Xue, L. Qu, H.-J. Choi, J.-B. Baek, Metal-free catalysts for oxygen reduction reaction, *Chem. Rev.* 115 (2015) 4823–4892.
- [14] J. Ying, J. Li, G. Jiang, Z.P. Cano, Z. Ma, C. Zhong, D. Su, Z. Chen, Metal-organic frameworks derived platinum-cobalt bimetallic nanoparticles in nitrogen-doped hollow porous carbon capsules as a highly active and durable catalyst for oxygen reduction reaction, *Appl. Catal. B* 225 (2018) 496–503.
- [15] Y. Hua, T. Jiang, K. Wang, M. Wu, S. Song, Y. Wang, P. Tsakarais, Efficient Pt-free electrocatalyst for oxygen reduction reaction: highly ordered mesoporous N and S co-doped carbon with saccharin as single-source molecular precursor, *Appl. Catal. B* 194 (2016) 202–208.
- [16] X. Liu, L. Dai, Carbon-based metal-free catalysts, *Nat. Rev. Mater.* 1 (2016) 16064.
- [17] L. Zhou, P. Fu, X. Cai, S. Zhou, Y. Yuan, Naturally derived carbon nanofibers as sustainable electrocatalysts for microbial energy harvesting: a new application of spider silk, *Appl. Catal. B* 188 (2016) 31–38.
- [18] T. Jiang, Y. Wang, K. Wang, Y. Liang, D. Wu, P. Tsakarais, S. Song, A novel sulfur-nitrogen dual doped ordered mesoporous carbon electrocatalyst for efficient oxygen reduction reaction, *Appl. Catal. B* 189 (2016) 1–11.
- [19] E. Bayram, G. Yilmaz, S. Mukerjee, A solution-based procedure for synthesis of nitrogen doped graphene as an efficient electrocatalyst for oxygen reduction reactions in acidic and alkaline electrolytes, *Appl. Catal. B* 192 (2016) 26–34.
- [20] Y. Jia, S. Haiyan, L. Haiyi, J. Hengxing, S. Li, G. Chao, X. Hangxun, A highly efficient metal-free oxygen reduction electrocatalyst assembled from carbon nanotubes and graphene, *Adv. Mater.* 28 (2016) 4606–4613.
- [21] Z. Li, S. Gadipelli, Y. Yang, Z. Guo, Design of 3D graphene-oxide spheres and their derived hierarchical porous structures for high performance supercapacitors, *Small* 13 (2017) 1702474.
- [22] Y. Lin, C. Guoliang, W. Zhenhai, Zn-MOF-74 derived N-doped mesoporous carbon as pH-Universal electrocatalyst for oxygen reduction reaction, *Adv. Funct. Mater.* 27 (2017) 1606190.
- [23] J. Li, M. Chen, D. Cullen, S. Hwang, M. Wang, B. Li, K. Liu, S. Karakalos, M. Lucero, H. Zhang, C. Lei, H. Xu, G. Sterbinsky, Z. Feng, D. Su, K. More, G. Wang, Z. Wang, G. Wu, Atomically dispersed manganese catalysts for oxygen reduction in proton-exchange membrane fuel cells, *Nat. Catal.* (2018), <https://doi.org/10.1038/s41929-018-0164-8>.
- [24] S. Guo, S. Zhang, L. Wu, S. Sun, Co/CoO Nanoparticles assembled on graphene for electrochemical reduction of oxygen, *Angew. Chem. Int. Ed.* 124 (2012) 11940–11943.
- [25] L. Feng, Y. Yan, Y. Chen, L. Wang, Nitrogen-doped carbon nanotubes as efficient and durable metal-free cathodic catalysts for oxygen reduction in microbial fuel cells, *Energy Environ. Sci.* 4 (2011) 1892–1899.
- [26] M. Borghei, N. Laucharoen, E. Kibena-Pöldsepp, L.-S. Johansson, J. Campbell, E. Kauppinen, K. Tammeveski, O. Rojas, Porous N, P-doped carbon from coconut shells with high electrocatalytic activity for oxygen reduction: Alternative to Pt-C for alkaline fuel cells, *Appl. Catal. B* 204 (2017) 394–402.
- [27] J. Deng, M. Li, Y. Wang, Biomass-derived carbon: synthesis and applications in energy storage and conversion, *Green Chem.* 18 (2016) 4824–4854.
- [28] W. Tian, H. Zhang, Z. Qian, T. Ouyang, H. Sun, J. Qin, M.O. Tadé, S. Wang, Bread-making synthesis of hierarchically Co@C nanoarchitecture in heteroatom doped porous carbons for oxidative degradation of emerging contaminants, *Appl. Catal. B* 225 (2018) 76–83.
- [29] Y. Guo, Z. Zeng, Y. Zhu, Z. Huang, Y. Cui, J. Yang, Catalytic oxidation of aqueous organic contaminants by persulfate activated with sulfur-doped hierarchically porous carbon derived from thiophene, *Appl. Catal. B* 220 (2018) 635–644.
- [30] H.-W. Liang, X. Zhuang, S. Brüller, X. Feng, K. Müllen, Hierarchically porous carbons with optimized nitrogen doping as highly active electrocatalysts for oxygen reduction, *Nat. Commun.* 5 (2014) 4973.
- [31] C. Zhu, H. Li, S. Fu, D. Du, Y. Lin, Highly efficient nonprecious metal catalysts towards oxygen reduction reaction based on three-dimensional porous carbon nanostructures, *Chem. Soc. Rev.* 45 (2016) 517–531.
- [32] G. Ferrero, K. Preuss, A. Marinovic, A. Jorge, N. Mansor, D. Brett, A. Fuertes, M. Sevilla, M.-M. Titirici, Fe–N-doped carbon capsules with outstanding electrochemical performance and stability for the oxygen reduction reaction in both acid and alkaline conditions, *ACS Nano* 10 (2016) 5922–5932.
- [33] A. Jain, R. Balasubramanian, M. Srinivasan, Hydrothermal conversion of biomass

- waste to activated carbon with high porosity: a review, *Chem. Eng. J.* 283 (2016) 789–805.
- [34] M. Borghesi, J. Lehtonen, L. Liu, O.J. Rojas, Advanced biomass-derived electrocatalysts for the oxygen reduction reaction, *Adv. Mater.* 30 (2018) 1703691.
- [35] L. Wang, X. Jiang, M. Zhang, M. Yang, Y.-N. Liu, In situ assembly of Au nanoclusters within protein hydrogel networks, *Chem. Asian J.* 12 (2017) 2374–2378.
- [36] T. Lin, I.-W. Chen, F. Liu, C. Yang, H. Bi, F. Xu, F. Huang, Nitrogen-doped mesoporous carbon of extraordinary capacitance for electrochemical energy storage, *Science* 350 (2015) 1508–1513.
- [37] D. Li, D. Yang, X. Yang, Y. Wang, Z. Guo, Y. Xia, S. Sun, S. Guo, Double-helix structure in carrageenan-metal hydrogels: a general approach to porous metal sulfides/carbon aerogels with excellent sodium-ion storage, *Angew. Chem. Int. Ed.* 55 (2016) 15925–15928.
- [38] B. You, F. Kang, P. Yin, Q. Zhang, Hydrogel-derived heteroatom-doped porous carbon networks for supercapacitor and electrocatalytic oxygen reduction, *Carbon* 103 (2016) 9–15.
- [39] Q. Ren, H. Wang, X.-F. Lu, Y.-X. Tong, G.-R. Li, Recent progress on MOF-derived heteroatom-doped carbon-based electrocatalysts for oxygen reduction reaction, *Adv. Sci.* 5 (2018) 1700515.
- [40] H.-W. Liang, Z.-Y. Wu, L.-F. Chen, C. Li, S.-H. Yu, Bacterial cellulose derived nitrogen-doped carbon nanofiber aerogel: an efficient metal-free oxygen reduction electrocatalyst for zinc-air battery, *Nano Energy* 11 (2015) 366–376.
- [41] D. Li, Y. Jia, G. Chang, J. Chen, H. Liu, J. Wang, Y. Hu, Y. Xia, D. Yang, X. Yao, A defect-driven metal-free electrocatalyst for oxygen reduction in acidic electrolyte, *Chem* 4 (2018) 2345–2356.
- [42] D. Li, Y. Jia, G. Chang, J. Chen, H. Liu, J. Wang, Y. Hu, Y. Xia, D. Yang, X. Yao, A defect-driven metal-free electrocatalyst for oxygen reduction in acidic electrolyte, *Chem* 4 (2018) 2345–2356.
- [43] J. Sheng, L. Wang, Y. Han, W. Chen, H. Liu, M. Zhang, L. Deng, Y.-N. Liu, Dual roles of protein as a template and a sulfur provider: a general approach to metal sulfides for efficient photothermal therapy of cancer, *Small* 14 (2018) 1702529.
- [44] L. Wang, K. Liang, X. Jiang, M. Yang, Y.-N. Liu, Dynamic protein–metal ion networks: a unique approach to injectable and self-healable metal sulfide/protein hybrid hydrogels with high photothermal efficiency, *Chem. Eur. J.* 24 (2018) 6557–6563.
- [45] L. Wang, L. Deng, Y.-N. Liu, Protein–metal-ion networks: a unique approach toward metal sulfide nanoparticles embedded in situ in nanocomposites, *Chem. Eur. J.* 24 (2018) 1–10.
- [46] D. Carter, J. Ho, Structure of serum albumin, *Adv. Protein Chem.* (1994) 153–203. Academic Press.
- [47] T. Topală, A. Bodoki, L. Opresan, R. Opresan, Bovine serum albumin interactions with metal complexes, *Clujul Med.* 87 (2014) 215–219.
- [48] S. Raja, T. Thiruselvi, A. Mandal, A. Gnanamani, pH and redox sensitive albumin hydrogel: a self-derived biomaterial, *Sci. Rep.* 5 (2015) 15977.
- [49] F. Shahid, J. Gomez, E. Birnbaum, D. Darnall, The lanthanide-induced N = to F transition and acid expansion of serum albumin, *J. Biol. Chem.* 257 (1982) 5618–5622.
- [50] D. Wu, Z. Chen, X. Liu, Study of the interaction between bovine serum albumin and ZnS quantum dots with spectroscopic techniques, *Spectrochim. Acta Part A* 84 (2011) 178–183.
- [51] H. Wang, D. Mitlin, J. Ding, Z. Li, K. Cui, Excellent energy–power characteristics from a hybrid sodium ion capacitor based on identical carbon nanosheets in both electrodes, *J. Mater. Chem. A* 4 (2016) 5149–5158.
- [52] D. Guo, R. Shibuya, C. Akiba, S. Saji, T. Kondo, J. Nakamura, Active sites of nitrogen-doped carbon materials for oxygen reduction reaction clarified using model catalysts, *Science* 351 (2016) 361–365.
- [53] C. Tang, H. Wang, X. Chen, B. Li, T. Hou, B. Zhang, Q. Zhang, M.-M. Titirici, F. Wei, Topological defects in metal-free nanocarbon for oxygen electrocatalysis, *Adv. Mater.* 28 (2016) 6845–6851.
- [54] Y. Lin, X. Pan, W. Qi, B. Zhang, D. Su, Nitrogen-doped onion-like carbon: a novel and efficient metal-free catalyst for epoxidation reaction, *J. Mater. Chem. A* 2 (2014) 12475–12483.
- [55] S.-H. Yoon, S. Lim, Y. Song, Y. Ota, W. Qiao, A. Tanaka, I. Mochida, KOH activation of carbon nanofibers, *Carbon* 42 (2004) 1723–1729.
- [56] R.-L. Tseng, S.-K. Tseng, Pore structure and adsorption performance of the KOH-activated carbons prepared from corn cob, *J. Colloid Interface Sci.* 287 (2005) 428–437.
- [57] I.-A. Choi, D.-H. Kwak, S.-B. Han, J.-Y. Park, H.-S. Park, K.-B. Ma, D.-H. Kim, J.-E. Won, K.-W. Park, Doped porous carbon nanostructures as non-precious metal catalysts prepared by amino acid glycine for oxygen reduction reaction, *Appl. Catal. B* 211 (2017) 235–244.
- [58] C. Tang, Q. Zhang, Nanocarbon for oxygen reduction electrocatalysis: dopants, edges, and defects, *Adv. Mater.* 29 (2017) 1604103.
- [59] J. Zhang, Z. Zhao, Z. Xia, L. Dai, A metal-free bifunctional electrocatalyst for oxygen reduction and oxygen evolution reactions, *Nat. Nanotechnol.* 10 (2015) 444–452.
- [60] X. Cui, Z. Pan, L. Zhang, H. Peng, G. Zhang, Selective etching of nitrogen-doped carbon by steam for enhanced electrochemical CO<sub>2</sub> reduction, *Adv. Energy Mater.* 7 (2017) 1701456.
- [61] W. Tian, H. Zhang, H. Sun, A. Suvorova, M. Saundar, M. Tade, S. Wang, Heteroatom (N or N-S)-doping induced layered and honeycomb microstructures of porous carbons for CO<sub>2</sub> capture and energy applications, *Adv. Funct. Mater.* 26 (2016) 8651–8661.
- [62] C. Hu, L. Dai, Multifunctional carbon-based metal-free electrocatalysts for simultaneous oxygen reduction, oxygen evolution, and hydrogen evolution, *Adv. Mater.* 29 (2017) 1604942.
- [63] L. Yang, X. Zeng, W. Wang, D. Cao, Recent progress in MOF-derived, heteroatom-doped porous carbons as highly efficient electrocatalysts for oxygen reduction reaction in fuel cells, *Adv. Funct. Mater.* 28 (2018) 1704537.
- [64] S. Gojković, S. Gupta, R. Savinell, Heat-treated iron(III) tetramethoxyphenyl porphyrin chloride supported on high-area carbon as an electrocatalyst for oxygen reduction: part II. Kinetics of oxygen reduction, *J. Electroanal. Chem. Lausanne* (Lausanne) 462 (1999) 63–72.
- [65] R. Jiang, F. Anson, The origin of inclined plateau currents in steady-state voltammograms for electrode processes involving electrocatalysis, *J. Electroanal. Chem. Interfacial Electrochem.* 305 (1991) 171–184.
- [66] B. Bozzini, P. Boccetta, G. Kourousias, A. Gianoncelli, Electrodeposition of Mn-Co/polypyrrole nanocomposites: an electrochemical and in situ soft-X-ray microscopic investigation, *Polymers* 9 (2017) 17.
- [67] D. Banham, S. Ye, K. Pei, J.-i. Ozaki, T. Kishimoto, Y. Imashiro, A review of the stability and durability of non-precious metal catalysts for the oxygen reduction reaction in proton exchange membrane fuel cells, *J. Power Sources* 285 (2015) 334–348.